

# EES Catalysis

Accepted Manuscript

This article can be cited before page numbers have been issued, to do this please use: J. Yang, L. Chen, X. Zhu, W. Shi, M. Huang, C. Liu, R. Ding, L. Gan and X. Yin, *EES Catal.*, 2025, DOI: 10.1039/D5EY00224A.



This is an Accepted Manuscript, which has been through the Royal Society of Chemistry peer review process and has been accepted for publication.

Accepted Manuscripts are published online shortly after acceptance, before technical editing, formatting and proof reading. Using this free service, authors can make their results available to the community, in citable form, before we publish the edited article. We will replace this Accepted Manuscript with the edited and formatted Advance Article as soon as it is available.

You can find more information about Accepted Manuscripts in the [Information for Authors](#).

Please note that technical editing may introduce minor changes to the text and/or graphics, which may alter content. The journal's standard [Terms & Conditions](#) and the [Ethical guidelines](#) still apply. In no event shall the Royal Society of Chemistry be held responsible for any errors or omissions in this Accepted Manuscript or any consequences arising from the use of any information it contains.

## Broader Context Statement

Hydrogen peroxide ( $\text{H}_2\text{O}_2$ )-mediated electrochemical reactions—including two-electron oxygen reduction ( $2\text{e}^-$ -ORR),  $\text{H}_2\text{O}_2$  oxidation (HPOR), and reduction (HPRR)—are pivotal for sustainable energy technologies, such as electrosynthesis of  $\text{H}_2\text{O}_2$  (a green oxidant and energy carrier), direct  $\text{H}_2\text{O}_2$  fuel cells, and regenerative energy storage systems. However, the efficiency of these interconnected reactions is fundamentally limited by the lack of universal activity descriptors and catalysts that can selectively drive target pathways while suppressing competing side reactions.

Here, we decouple the structure-activity relationships of Co- $\text{N}_4$  single-atom catalysts with defined coordination environments (pyrrolic *vs.* pyridinic) for all three  $\text{H}_2\text{O}_2$ -related reactions. We demonstrate that the conventional descriptor ( $\Delta G_{\text{OOH}}^*$ ) fails to predict HPRR activity, which is governed by  $\text{H}_2\text{O}_2$  adsorption configurations and dissociation kinetics instead. This work provides design principles for on-demand catalysts tailored to specific  $\text{H}_2\text{O}_2$  energy applications—enabling efficient  $\text{H}_2\text{O}_2$  electrosynthesis, high-power fuel cells, and closed-loop  $\text{H}_2\text{O}_2$ -based energy storage.



# Structure-activity relationship in Co-N-C catalysts for multiple H<sub>2</sub>O<sub>2</sub>-related electrochemical reactions

Jie Yang<sup>a,b</sup>, Lifang Chen<sup>a\*</sup>, Xuya Zhu<sup>c</sup>, Wenwen Shi<sup>a</sup>, Mengxue Huang<sup>a,b</sup>, Chang Liu<sup>a,b</sup>, Ruimin Ding<sup>a\*</sup>, Lin Gan<sup>c\*</sup>, Xi Yin<sup>a\*</sup>

<sup>a</sup>State Key Laboratory of Coal Conversion, Institute of Coal Chemistry, Chinese Academy of Sciences; Taiyuan, Shanxi 030001, China.

<sup>b</sup>School of Chemical Engineering, University of Chinese Academy of Sciences; Beijing 100049, China.

<sup>c</sup>Tsinghua Shenzhen International Graduate School, Tsinghua University, Shenzhen 518055, China

\*Corresponding authors. Email: chenlifang@sxicc.ac.cn; dingrm@sxicc.ac.cn; lgan@sz.tsinghua.edu.cn; xiyin@sxicc.ac.cn

View Article Online  
DOI: 10.1039/D5EY00224A



## Abstract

H<sub>2</sub>O<sub>2</sub>-related electrochemical reactions, including two-electron oxygen reduction reaction (2e-ORR), H<sub>2</sub>O<sub>2</sub> oxidation reaction (HPOR), and H<sub>2</sub>O<sub>2</sub> reduction reaction (HPRR), have received significant attention for the electrosynthesis of H<sub>2</sub>O<sub>2</sub> and energy storage. Understanding the complex structure-activity relationships among 2e-ORR/HPOR/HPRR and their connections is crucial for further developing highly efficient catalysts and working systems. Herein, we unveil these intricacies by employing model Co-N-C catalysts with well-defined active site configuration (Co-N<sub>4</sub>-pyrrolic and Co-N<sub>4</sub>-pyridinic) in a combined experimental and computational approach. We report the higher 2e-ORR/HPOR but lower HPRR activity of the CoN<sub>4</sub>-pyrrolic site than the CoN<sub>4</sub>-pyridinic site based on their reaction free energy landscapes remodeled considering the chemisorption steps of O<sub>2</sub> and H<sub>2</sub>O<sub>2</sub>. The results reveal that the binding free energy of \*OOH ( $\Delta G_{*OOH}$ ) can only be utilized as a reliable descriptor for 2e-ORR/HPOR activity, but not indicative of HPRR activity, regardless of the scaling relationship of the common reaction intermediates (\*OOH or \*OH). The HPRR activity of CoN<sub>4</sub> sites strongly depends on the H<sub>2</sub>O<sub>2</sub> adsorption strength and configuration. These findings provide valuable insights into the design of catalysts for H<sub>2</sub>O<sub>2</sub>-related electrochemical energy conversion and storage systems.

**Keywords:** Structure-activity relationship, activity descriptor, two-electron oxygen reduction reaction, hydrogen peroxide oxidation reaction, hydrogen peroxide reduction reaction, single atom catalyst

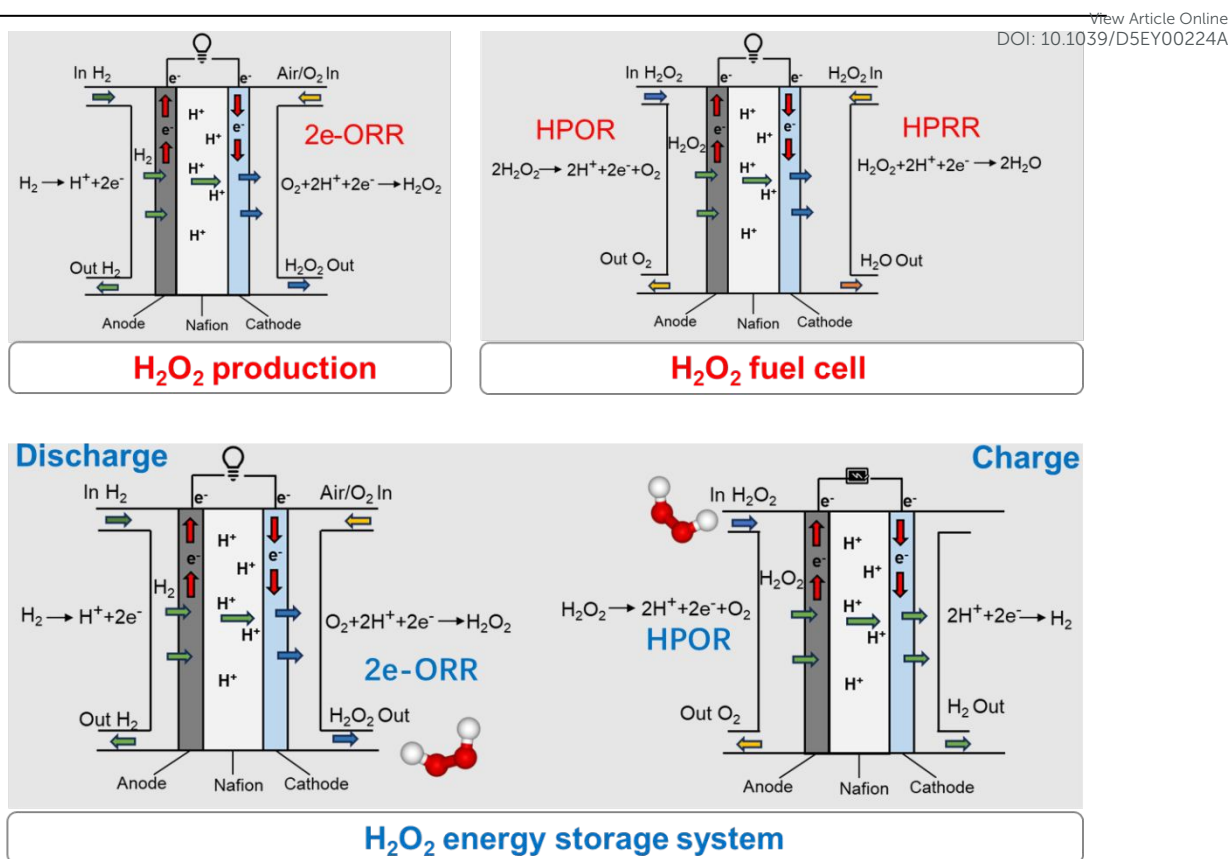


## 1. Introduction

View Article Online  
DOI: 10.1039/D5EY00224A

Hydrogen peroxide ( $\text{H}_2\text{O}_2$ )-related electrochemical reactions, including two-electron oxygen reduction reaction (2e-ORR),  $\text{H}_2\text{O}_2$  oxidation reaction (HPOR), and  $\text{H}_2\text{O}_2$  reduction reaction (HPRR), have received significant attention for their key roles in the  $\text{H}_2\text{O}_2$  electrosynthesis,<sup>1-5</sup> fuel cells,<sup>6-10</sup> and energy storage systems.<sup>11-14</sup> These reactions often couple with each other positively or negatively, depending on the specific applications (**Scheme 1**). For instance, at the 2e-ORR electrode for  $\text{H}_2\text{O}_2$  electrosynthesis, the undesired HPRR often occurs and consumes the valuable product.<sup>15,16</sup> Conversely, in the cathode of hydrogen fuel cells, the HPRR can convert harmful  $\text{H}_2\text{O}_2$  into water, thereby enhancing stability and efficiency.<sup>17,18</sup> The 2e-ORR and its reverse reaction, HPOR, facilitate the electrochemical cycle of  $\text{H}_2\text{O}_2$ , offering potential applications in energy and hydrogen storage.<sup>11</sup> In the case of an  $\text{H}_2\text{O}_2$  electrolyzer for power-to- $\text{H}_2$  conversion, the coupling of HPRR with HPOR at the anode reduces the  $\text{H}_2\text{O}_2$  utilization and energy efficiency of the system.<sup>13,14</sup> Furthermore, HPOR and HPRR can be employed in driving the direct- $\text{H}_2\text{O}_2$  fuel cells at the anode and cathode, respectively.<sup>6-10</sup> To date, the mechanistic studies of 2e-ORR,<sup>2,19,20</sup> HPOR,<sup>11,14,21,22</sup> and HPRR<sup>23-26</sup> are often conducted independently rather than being fully integrated. Given the significance of these reactions and their intricate relationships in various applications, understanding their comprehensive connections is imperative for the advancement of highly efficient catalysts and operational systems.





**Scheme 1.** Critical roles of H<sub>2</sub>O<sub>2</sub>-related electrochemical reactions, including 2e-ORR, HPOR, and HPRR, for various applications.

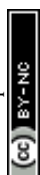
Among these reactions, 2e-ORR and HPOR share the same intermediate of adsorbed hydroperoxyl (\*OOH, where \* denotes the catalytic site), and the HPRR involves an intermediate of adsorbed hydroxyl (\*OH).<sup>2,13,27-30</sup> The binding free energies of these intermediates, namely  $\Delta G_{*OOH}$  and  $\Delta G_{*OH}$ , have been proposed as the thermodynamic activity descriptors for the above reactions.<sup>31-34</sup> Considering the established scaling relationship between  $\Delta G_{*OOH}$  and  $\Delta G_{*OH}$  for various catalyst types ( $\Delta G_{*OOH} = \Delta G_{*OH} + 3.2 \pm 0.2$  eV), there may be an intrinsic correlation among the 2e-ORR, HPOR, and HPRR (2e-ORR/HPOR/HPRR) processes.

Cobalt and nitrogen-doped carbon (Co-N-C), specifically those with nitrogen-coordinated cobalt (CoN<sub>x</sub>) sites, have demonstrated activities across all three H<sub>2</sub>O<sub>2</sub>-related reactions.<sup>11,15,35</sup> For instance, Dodelet *et al.* observed that Co-N-C is a



remarkable catalyst for both HPOR and HPRR.<sup>35</sup> And Strasser *et al.* found that Co-N-C exhibits high 2e-ORR selectivity and low HPRR activity, contributing significantly to H<sub>2</sub>O<sub>2</sub> productivity.<sup>15</sup> However, there is a discrepancy in the HPRR activity of the Co-N-C catalyst between these findings, possibly due to differences in the coordination environment around the Co ions. A recent study combining theoretical simulation and experiments identified that pyrrolic-type CoN<sub>4</sub> (CoN<sub>4</sub>-pyrrolic) is mainly responsible for the 2e-ORR, while pyridinic-type CoN<sub>4</sub> (CoN<sub>4</sub>-pyridinic) catalyzes the 4e-ORR.<sup>36</sup> This highlights the significance of the coordination environment around Co ions for its catalytic properties. Through precise control of the coordination environment of Co, we could gain fundamental insights into the structure-activity relationship between CoN<sub>4</sub> and the 2e-ORR/HPOR/HPRR, opening opportunities to find a correlation among these reactions.

Herein, we employ Co-N-C catalysts with CoN<sub>4</sub>-pyridinic and CoN<sub>4</sub>-pyrrolic sites to establish the structure-activity relationships for 2e-ORR/HPOR/HPRR, examining the underlying connections among these reactions. The catalyst characterization and performance evaluation confirm that the CoN<sub>4</sub>-pyrrolic site exhibits higher 2e-ORR and HPOR activity but lower HPRR activity compared to the CoN<sub>4</sub>-pyridinic site. The results from density functional theory (DFT) calculations predict the same active site structural dependency for these reactions. The chemical process involving H<sub>2</sub>O<sub>2</sub> determines the HPRR activity while the  $\Delta G^*_{\text{OOH}}$  determines the 2e-ORR/HPRR activity. The activity of 2e-ORR and HPOR can be accurately predicted using a single thermodynamic descriptor. While HPRR follows chemical-electrochemical mechanisms, predicting its activity requires an in-depth analysis of the reaction pathway. This work advances the field by providing the first systematic investigation of three distinct H<sub>2</sub>O<sub>2</sub> reaction pathways across differently coordinated CoN<sub>4</sub> motifs, while rigorously evaluating the universality of conventional activity descriptors through both theoretical and experimental validation. These valuable insights into the H<sub>2</sub>O<sub>2</sub>-related reactions can



guide the development of high-performance catalysts for various  $\text{H}_2\text{O}_2$ -based energy applications.

## 2. Experimental Section

### 2.1 Materials

Cobalt chloride ( $\text{CoCl}_2$ , 99.7%, anhydrous, Aladdin Biochemical Technology Co.), cobalt(II) acetate tetrahydrate ( $\text{Co}(\text{CH}_3\text{COO})_2 \cdot 4\text{H}_2\text{O}$ , 98%, Sigma Aldrich), Zinc acetate dihydrate ( $\text{Zn}(\text{CH}_3\text{COO})_2 \cdot 2\text{H}_2\text{O}$ , analytical reagent grade, Aladdin Biochemical Technology Co.), aniline (98%, Sigma-Aldrich), hydrogen peroxide ( $\text{H}_2\text{O}_2$ , 30 wt%, Alfa Aesar), 2-methylimidazole (2-MIM,  $\text{C}_4\text{H}_6\text{N}_2$ , 98%, Aladdin Biochemical Technology Co.), tannic acid (TA, analytical reagent grade, Aladdin Biochemical Technology Co.), hydrochloric acid ( $\text{HCl}$ , 36-38 wt%, analytical reagent grade, SCR, China), nitric acid ( $\text{HNO}_3$ , 65-68 wt%, analytical reagent grade, SCR, China), sulfuric acid ( $\text{H}_2\text{SO}_4$ , 95-98 wt%, analytical reagent grade, SCR, China), APS (98%, Sigma-Aldrich), isopropanol (IPA, >99.7%, analytical reagent grade; Kermel, SCR, China), methanol ( $\text{CH}_3\text{OH}$ , analytical reagent grade, SCR, China), deionized water (DI-water, Milli-Q, 18.2  $\text{M}\Omega$  cm at 25 °C), ultrapure  $\text{N}_2$  (99.999%), ultrapure  $\text{O}_2$  (99.999%), carbon black (BlackPearl 2000, Cabot Co.), 20 wt% Pt/C (Hispec3000, Johnson Matthey Co.) and a D521 Nafion dispersion (5 wt%, EW = 1100, Chemours) were utilized as received.

### 2.2 Preparation of catalysts

The Co-N-C catalyst, featuring  $\text{CoN}_{4\text{-pyrrolic}}$  dominated coordination ( $\text{CoN}_{\text{pyr}}\text{C}$ ), was prepared by heating a precursor mixture containing  $\text{CoCl}_2$ , polymerized aniline, and oxidized carbon black (OCB). Aniline (1.024 g, 8.11 mmol) was added to 200 mL of 1 M  $\text{HCl}$  under continuous magnetic stirring to form a monomer solution. Separately, a second solution was prepared by adding 1.246 g of 30 wt%  $\text{H}_2\text{O}_2$  solution (11 mmol  $\text{H}_2\text{O}_2$ ) and 7.141 g of  $\text{CoCl}_2$  (55 mmol) to 200 mL of 1 M  $\text{HCl}$ . This second solution was then introduced into the aniline solution to initiate the polymerization process. The resulting mixture was maintained at room temperature with constant magnetic stirring





at 60 rpm for 4 h. Concurrently, a dispersion of OCB was prepared by sonicating 0.20 g of OCB in a mixture of 100 mL H<sub>2</sub>O and 10 mL IPA. The OCB dispersion was then added to the polymer dispersion under stirring at 600 rpm. After 24 h, the combined dispersion was heated to 80 °C and concentrated under continuous stirring at 600 rpm to yield a dark slurry. Then, the slurry was loaded into an alumina combustion boat and heat-treated at 900 °C in a tube furnace in N<sub>2</sub> under ambient pressure. The ramping rate was 30 °C/min, and the holding time at 900 °C was 1 h. Finally, the pyrolyzed material was ground into a fine powder using an agate mortar and pestle and treated with a 12 N HCl solution for 24 h to remove spectator Co-rich phases. The acid-leached sample was washed with DI water and dried under vacuum at 60 °C. The final product was obtained after the second heat treatment at 900 °C for 3 h in flowing N<sub>2</sub> with a ramping rate of 30 °C/min.

The N<sub>pyrr</sub>C refers to the blank N-doped carbon matrices that replicate the morphological features of the CoN<sub>pyrr</sub>C but are intentionally devoid of CoN<sub>4</sub> coordination sites. Its synthesis follows a similar procedure to that of CoN<sub>pyrr</sub>C but without adding the CoCl<sub>2</sub>.

The Co-N-C catalyst, featuring CoN<sub>4</sub>-pyridinic dominated coordination (CoN<sub>py</sub>C), was synthesized by heat treatment of the ZIF-67 material obtained by reacting acetate with 2-MIM. First, Zn(CH<sub>3</sub>COO)<sub>2</sub>·2H<sub>2</sub>O (1 mmol) and Co(CH<sub>3</sub>COO)<sub>2</sub>·4H<sub>2</sub>O (1 mmol) were dissolved in 5 mL of H<sub>2</sub>O to form a clear pink solution, which was subsequently added to 5 mL of H<sub>2</sub>O containing 2-MIM (13.6 mmol) under stirring at room temperature. The resulting mixture turned purple after a few seconds and was left undisturbed at room temperature for 4 h, then washed three times with DI-water to obtain ZIF-67. Then, the prepared ZIF-67 was etched with 50 mL TA solution (5 mg/mL) while stirring for 20 min. The products were washed with water and methanol and then dried in an oven at 80 °C. Finally, the dried powder was loaded into an alumina combustion boat and heat-treated at 900 °C (5 °C/min) in a tube furnace in N<sub>2</sub> at ambient pressure. The holding time at 900 °C was 2 h.



The  $N_{py}C$  refers to the blank N-doped carbon matrices that mimic the morphological features of the  $CoN_{py}C$  but lack  $CoN_4$  coordination sites. Its synthesis is similar to that of the  $CoN_{py}C$  but without the incorporation of the  $Co(CH_3COO)_2 \cdot 4H_2O$ .

### 2.3 Physical characterizations

The Co-N-C catalysts were characterized using a scanning electron microscope (SEM, JSM-7001F, Japan) operated at an accelerating voltage of 80 kV and a high-resolution transmission electron microscope (TEM, JEM-2100F, JEOL, Japan). Powder X-ray diffraction (XRD, D8 ADVANCE A25, Bruker Co., USA) patterns were recorded using a Bruker D8-Advance-A25 diffractometer with Cu  $K\alpha$  radiation over a  $2\theta$  range from  $5^\circ$  to  $90^\circ$ . Raman spectra were recorded on a LabRAM HR Evolution (HORIBA Scientific, France) using a 514 nm laser as the excitation source. The X-ray photoelectron spectroscopy (XPS, Axis Ultra DLD, Kratos Analytical Ltd, UK) was performed on a monochromatic Al  $K\alpha$  source at 150 W without charge compensation. Cobalt K-edge X-ray Co K-edge X-ray absorption spectroscopy (XAS) was measured at the XRD station of beamline 4B9A of Beijing Synchrotron Radiation Facility (BSRF) in transmission or fluorescence mode.

### 2.4 Electrochemical measurements

The electrochemical activities of 2e-ORR were measured at ambient temperature ( $25 \pm 2^\circ C$ ) in a five-necked electrochemical cell filled with a 0.5 M  $H_2SO_4$  electrolyte employing a bipotentiostat (CHI 760E; CH Instruments, Inc.). A rotating ring-disc electrode (RRDE, Pine Research Instrumentation) with a glassy carbon disk ( $\Phi = 5.50$  mm, area =  $0.2375\text{ cm}^2$ ) and a Pt ring was employed as the working electrode, whereas a graphite rod and reversible hydrogen electrode (RHE) were employed as the counter and reference electrodes, respectively. Catalyst ink was prepared by dispersing 5 mg of the catalyst powder in 500  $\mu L$  of DI water. Subsequently, 500  $\mu L$  of IPA was added, followed by the addition of 12  $\mu L$  of Nafion D521 dispersion. The mixture was then sonicated in an ice-water bath for 1 h to ensure homogeneity. Subsequently, to prepare the electrodes, 4.7  $\mu L$  of the ink was deposited onto the GCE, resulting in a catalyst



loading of 0.1 mg/cm<sup>2</sup>. Uniform catalyst coating on the GCE was achieved by slow drying under rotation.

Their cyclic voltammograms (CVs) were recorded from 0 to 1.0 V vs. RHE in an N<sub>2</sub>-saturated 0.5 M H<sub>2</sub>SO<sub>4</sub> solution at a scan rate of 50 mV/s. The 2e-ORR performance was measured in O<sub>2</sub>-saturated 0.5 M H<sub>2</sub>SO<sub>4</sub> (O<sub>2</sub> purged for ≥ 30 min) under steady-state conditions by polarizing the working electrode from 1.0 to 0 V vs. RHE employing 20 mV potential steps and a hold time of 20 s at each step. The rotation rate was 900 rpm. The ring current was measured at a ring potential of 1.3 V vs. RHE, and the current collection coefficient of the ring electrode (*N*) was 0.38. The electrochemical surface areas (ECSA) of the catalyst were calculated from the equation:

$$ECSA = \frac{Q}{C_s \Delta E m} \quad Eq.1$$

where *Q* is integrated double-layer charge (mC) measured in CV over a 0-1.0 V vs. RHE, *C<sub>s</sub>* is the specific double-layer capacitance (30 μF/cm<sup>2</sup>), *ΔE* is the width of the potential window (1.0 V), and *m* is the catalyst mass loading on the electrode (mg).

Electron transfer number (*n*) and H<sub>2</sub>O<sub>2</sub> yield (*Y*<sub>H<sub>2</sub>O<sub>2</sub></sub>) were calculated using the following equations:

$$n = \frac{4I_d}{\left(I_d + \frac{I_r}{N}\right)} \quad Eq.2$$

$$Y_{H_2O_2} = 200\% \frac{\left(\frac{I_r}{N}\right)}{\left(I_d + \frac{I_r}{N}\right)} \quad Eq.3$$

where *I<sub>d</sub>* and *I<sub>r</sub>* are the disk and ring currents, respectively.

The electrochemical activities of HPOR/HPRR were measured by a bipotentiostat (CHI 760E) in an H-type electrolysis cell. A proton exchange membrane (Nafion® NR211) was used to separate the two compartments of the H-cell. A glassy carbon rotating disk electrode (RDE) (*Φ* = 5.00 mm, area = 0.1963 cm<sup>2</sup>) and an Ag/AgCl (KCl, 3 M) reference electrode were placed in one cell compartment, which was filled with 0.5 M H<sub>2</sub>SO<sub>4</sub> and 0.5 M H<sub>2</sub>O<sub>2</sub>. At the same time, a graphite rod counter electrode was



positioned in the other compartment that was filled with 0.5 M H<sub>2</sub>SO<sub>4</sub>. Catalysts loaded at 0.1 mg/cm<sup>2</sup> were prepared by depositing 3.9 μL of ink onto the GCE. CVs were recorded from 0.4 to 1.0 V vs. RHE in an N<sub>2</sub>-saturated 0.5 M H<sub>2</sub>SO<sub>4</sub> and 0.5 M H<sub>2</sub>O<sub>2</sub> solution at a scan rate of 50 mV/s. The rotation rate was 900 rpm.

The kinetically limited current density ( $j_k$ ) was determined using the Koutecký-Levich equation:

$$\frac{1}{j} = \frac{1}{j_k} + \frac{1}{j_d} \quad \text{Eq.4}$$

where  $j$  is the measured current density and  $j_d$  is the diffusion-limited current density.

The diffusion-limited current density is governed by the equation:

$$j_d = 0.62nFC_{H_2O_2}D_{H_2O_2}^{\frac{2}{3}}\nu^{-\frac{1}{6}}\omega^{\frac{1}{2}} \quad \text{Eq.5}$$

where  $n$  is the stoichiometric number of electrons transferred in the HPOR/HPRR,  $F$  is the Faraday constant,  $C_{H_2O_2}$  is the concentration of dissolved H<sub>2</sub>O<sub>2</sub> (0.5 M),  $D_{H_2O_2}$  is the diffusion coefficient (1.3×10<sup>-5</sup> cm<sup>2</sup>/s),  $\nu$  is the kinetic viscosity of the solution (0.009 cm<sup>2</sup>/s), and  $\omega$  is the rotation rate of the disc electrode (900 rpm).

The logarithm of the current density ( $j_k$ ) was plotted against the potential to obtain a semilogarithmic polarization curve, also known as a Tafel plot. The linear part of this curve was fitted using the equation:

$$\eta = a + b \log j_k \quad \text{Eq.6}$$

where  $\eta$  is the overpotential,  $a$  is the intercept at the x-axis when  $\eta = 0$ ,  $b$  is the Tafel slope, and  $j$  is the average of the forward and reverse scan current density in CV.

Mass activity (MA) and specific activity (SA) were quantified through the following equations:

$$MA = \frac{j_k}{m} \quad \text{Eq.7}$$

$$SA = \frac{MA}{ECSA} \quad \text{Eq.8}$$

## 2.5 Computational details



All spin-polarized density functional theory (DFT) calculations were performed using the GGA-PBE functional in the VASP 5.4.4 code.<sup>37-39</sup> The core-valence interactions were described using the projector augmented wave (PAW) pseudopotential,<sup>40,41</sup> with a plane-wave basis set truncated at a cut-off energy of 400 eV. The van der Waals (vdW) interactions were incorporated through the empirical Grimme's DFT-D3 method.<sup>42</sup> The k-point grids were set to be  $4 \times 4 \times 1$  by the Monkhorst–Pack method. Geometric optimizations employed the conjugate gradient algorithm, with force and energy convergence criteria set to 0.01 eV/Å and  $10^{-5}$  eV, respectively. A 15 Å vacuum layer was set to avoid interactions.

The chemical potential of the  $H^+/e^-$  pair is equal to half of the gas-phase  $H_2$  at standard hydrogen electrode (SHE) conditions from the computational hydrogen electrode (CHE).<sup>43</sup> All free energies were calculated relative to  $H_2O(l)$  and  $H_2(g)$ .

The free energy ( $G$ ) for each reaction intermediate was calculated as:

$$G = E_{\text{DFT}} + \text{ZPE} - TS + E_{\text{sol}} \quad \text{Eq.9}$$

where  $E_{\text{DFT}}$  is the total energy by DFT calculation, ZPE is the zero-point energy,  $S$  is the entropy, and  $T$  is the temperature (298.15 K, in our work). For adsorbed reaction intermediates, their ZPE and  $S$  were obtained via vibrational frequency computations.  $E_{\text{sol}}$  is an implicit solvation correction of  $\sim 0.3$  eV for the adsorption free energies.<sup>44</sup>

The adsorption free energies of \*OOH, \*OH, and \*O were defined as follows:

$$\Delta G(*\text{OOH}) = G(*\text{OOH}) - G(*) - 2G(\text{H}_2\text{O}) + 3/2G(\text{H}_2) \quad \text{Eq.10}$$

$$\Delta G(*\text{OH}) = G(*\text{OH}) - G(*) - G(\text{H}_2\text{O}) + \frac{1}{2}G(\text{H}_2) \quad \text{Eq.11}$$

$$\Delta G(*\text{O}) = G(*\text{O}) - G(*) - G(\text{H}_2\text{O}) + G(\text{H}_2) \quad \text{Eq.12}$$

where  $\Delta G(*\text{OOH})$ ,  $\Delta G(*\text{OH})$ , and  $\Delta G(*\text{O})$  are the adsorption free energies of OOH, OH, and O intermediate, respectively.  $G(*)$  is the energy of a clean surface.  $G(*\text{OOH})$ ,  $G(*\text{OH})$ , and  $G(*\text{O})$  are the free energies of intermediate (OOH, OH, and O) adsorbed on the surface.  $G(\text{H}_2\text{O}(l))$  and  $G(\text{H}_2(g))$  are the energies of free  $\text{H}_2\text{O}(l)$  and  $\text{H}_2(g)$ .





### 3. Results and discussion

#### 3.1 Co-N-C catalysts with CoN<sub>4</sub>-pyrrolic and CoN<sub>4</sub>-pyridinic active sites

We synthesized Co-N-C catalysts with dominant CoN<sub>4</sub>-pyrrolic sites (CoN<sub>pyrr</sub>C catalyst) and CoN<sub>4</sub>-pyridinic sites (CoN<sub>py</sub>C catalyst) using separate methods (**Figure 1a**).<sup>45,46</sup> Briefly, the CoN<sub>pyrr</sub>C catalyst was prepared by heat-treatment of a precursor mixture containing cobalt (II) chloride, polyaniline (PANI), and oxidized carbon black (OCB).<sup>45</sup> The CoN<sub>py</sub>C catalyst was synthesized by heat-treatment of ZIF-67 material obtained by reacting cobalt (II) acetate with 2-methylimidazole (2-MIM).<sup>46</sup>

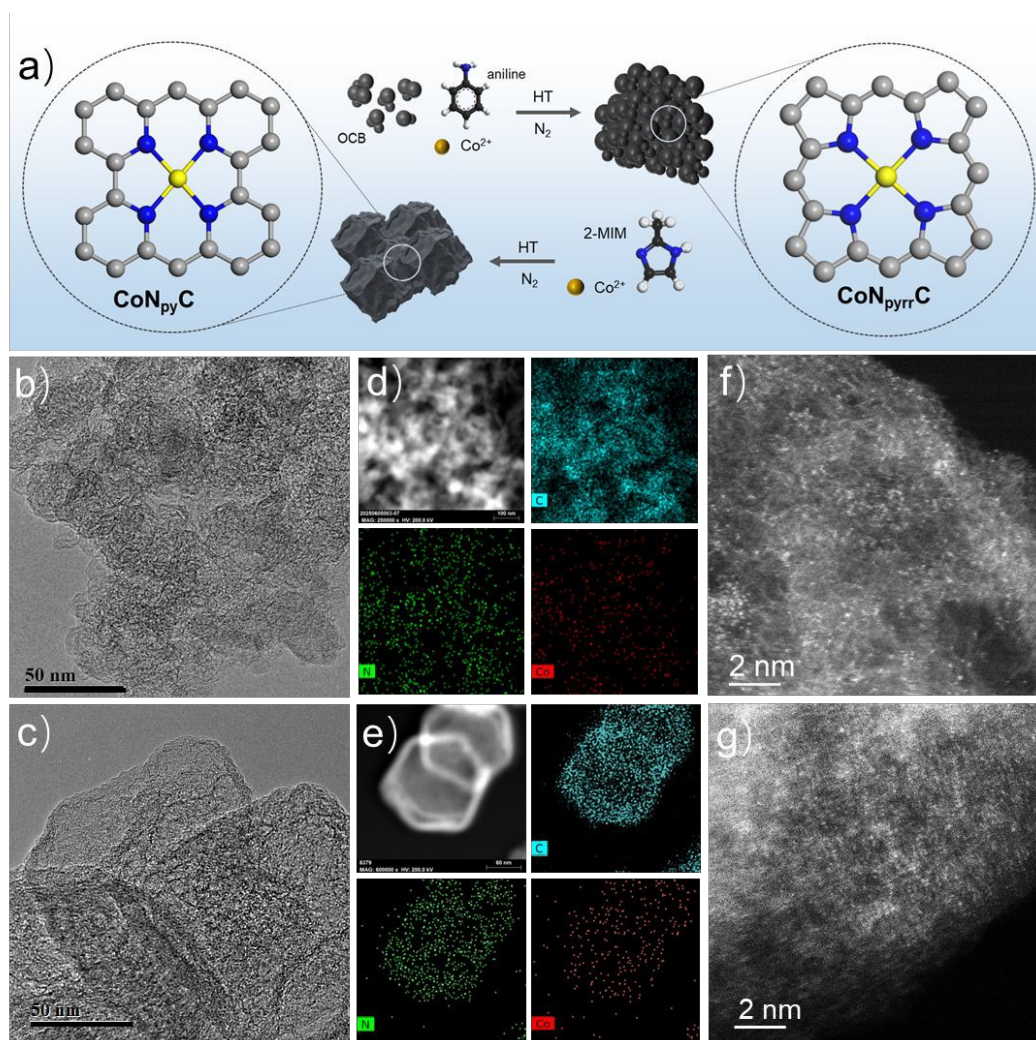


**Figure 1.** a) Schematic synthesis routes for the Co-N-C catalysts with different coordination structures. b, c) TEM images; d, e) element mapping images; and f, g) HAADF-STEM images of the CoN<sub>pyrr</sub>C and CoN<sub>py</sub>C catalysts, respectively.

The structural and elemental analysis results indicate that both catalysts are primarily carbon matrices doped with dispersed Co and N elements. Specifically, XRD patterns of both catalysts display a graphite-type phase, evident by two distinct characteristic peaks at 26.54° and 43.28° corresponding to the (002) and (101) planes of graphite (PDF #75–1621), respectively (**Figure S1a**). No peaks indicative of cobalt-rich phases were observed. Their Raman spectra (**Figure S1b**) share a similar ratio of D-band (disordered carbon, at *ca.* 1350 cm<sup>-1</sup>) to G-band (graphitic carbon, at *ca.* 1580 cm<sup>-1</sup>) with I<sub>D</sub>:I<sub>G</sub> of 1.07 and 1.08, respectively, indicating comparable disordered graphitic structures. SEM and TEM (**Figure 1b-c** and **Figure S1c-d**) micrographs show that the CoN<sub>pyrr</sub>C catalyst exhibits an amorphous carbon particle morphology, while the CoN<sub>py</sub>C catalyst displays a hollow dodecahedral structure with a concave shell. EDS elemental mapping (**Figure 1d-e**) indicates the distinguishable signals of C, N, and Co, revealing uniform dispersion of Co within the carbon matrix. HAADF-STEM images show bright and isolated spots (**Figure 1f-g**), indicative of atomically dispersed Co sites in both catalysts.

The N 1s XPS spectra for the CoN<sub>pyrr</sub>C and CoN<sub>py</sub>C (**Figure 2a**) can be fitted with four main types of N species, including pyridinic-N (398.6 eV), pyrrolic-N (400.3 eV), graphitic-N (401.3 eV), and oxidized-N (403.2 eV) species.<sup>36, 47, 48</sup> The fitting results (**Figure 2b** and **Table S1**) show that the CoN<sub>pyrr</sub>C catalyst has a higher proportion of pyrrolic-N (*ca.* 45 at%) compared to pyridinic-N (*ca.* 22 at%). Conversely, the CoN<sub>py</sub>C predominantly contains pyridinic-N species (*ca.* 52 at%) with a low fraction of pyrrolic-N (*ca.* 14 at%). Assuming that atomically dispersed Co is randomly coordinated with pyridinic- or pyrrolic-N sites, and considering their favorable thermodynamic



formation energies,<sup>36,49</sup> the probability of CoN<sub>4</sub> sites in CoN<sub>4</sub>-pyrrolic or CoN<sub>4</sub>-pyridinic configurations is 67% vs. 33% in CoN<sub>pyrr</sub>C, and 79% vs. 21% in CoN<sub>py</sub>C catalyst.

To further investigate the oxidation state and local coordination environment of the Co ions at the atomic level, Co K-edge XAS measurements were conducted. For comparative purposes, Co foil and cobalt phthalocyanine (CoPc) were also analyzed. We acknowledge the lack of a well-defined pyridinic-CoN<sub>4</sub> reference material for direct XAS comparison. The Co K-edge X-ray absorption near-edge structure (XANES) spectra (**Figure 2c**) show that both CoN<sub>pyrr</sub>C and CoN<sub>py</sub>C exhibit a higher pre-edge adsorption energy at the energy half of the edge maximum intensity compared to Co foil, indicating a positive valency of Co in the catalysts.<sup>36,50,51</sup> The XANES spectrum of CoPc shows a sharp pre-edge peak at 7712 eV (peak B), indicative of the square-planar symmetry (D<sub>4h</sub>) of the CoN<sub>4</sub> structure (Figure 2c).<sup>45,47,52</sup>

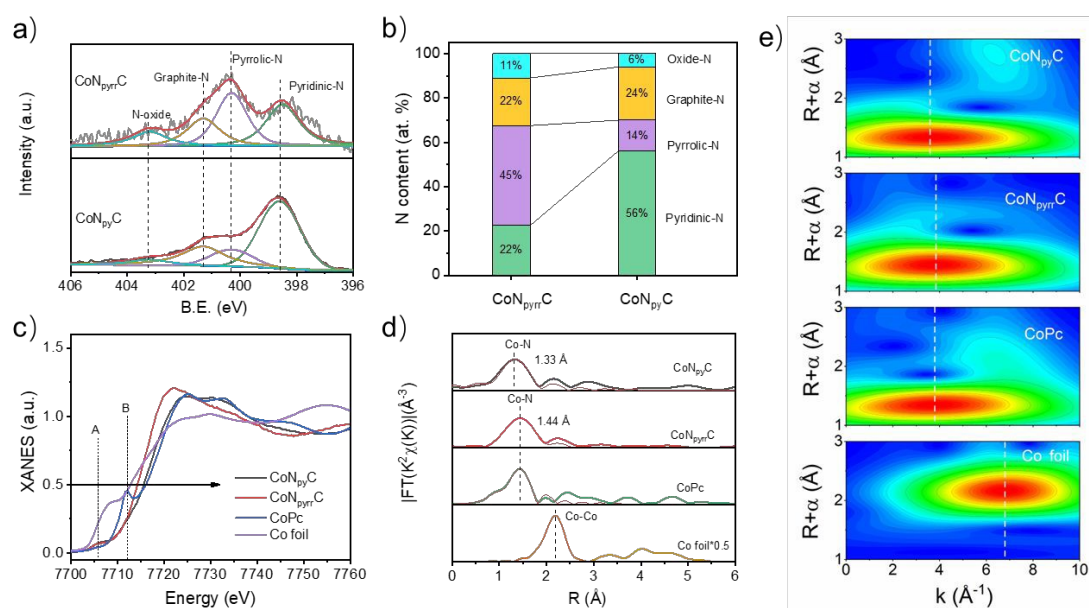


**Figure 2.** a) N 1s XPS spectra, and b) proportion of different N species for the CoN<sub>pyrr</sub>C and CoN<sub>py</sub>C. c) Co K-edge XANES spectra, d) FT  $k^2$ -weighted and fitting EXAFS spectra, and e) WT  $k^2$ -weighted EXAFS contour plots of the CoN<sub>pyrr</sub>C, CoN<sub>py</sub>C, and other reference sample.



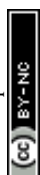


In contrast,  $\text{CoN}_{\text{pyrr}}\text{C}$  and  $\text{CoN}_{\text{py}}\text{C}$  lack peak B, but instead, feature a peak at 7706 eV (peak A), attributable to the distorted local structures of atomically dispersed  $\text{CoN}_4$  sites. The presence of peak A confirms the existence of the  $\text{CoN}_4$  site structure within the  $\text{CoN}_{\text{pyrr}}\text{C}$  and  $\text{CoN}_{\text{py}}\text{C}$  catalysts.

The Fourier-transform (FT) of Co K-edge extended X-ray absorption fine structure (FT-EXAFS) spectra (**Figure 2d**) confirms the absence of Co-Co bonds (2.17 Å) in  $\text{CoN}_{\text{pyrr}}\text{C}$  and  $\text{CoN}_{\text{py}}\text{C}$ , consistent with the HAADF-STEM images. The prominent peaks at 1.44 Å for  $\text{CoN}_{\text{pyrr}}\text{C}$  and CoPc point to the  $\text{CoN}_{4\text{-pyrrolic}}$  structure, whereas the prominent peak at 1.33 Å for  $\text{CoN}_{\text{py}}\text{C}$  aligns well with the  $\text{CoN}_4$  structures featuring a pyridinic-N configuration reported in the literature.<sup>36,53</sup> To further confirm this analysis, we performed a least-square curve fitting analysis for the first coordination shell of Co (**Figures S2-S5**). The fitted coordination numbers for the  $\text{CoN}_{\text{pyrr}}\text{C}$  and  $\text{CoN}_{\text{py}}\text{C}$  are 3.99 and 4.02 (**Table S2**), respectively. And the fitted bond lengths of Co-N in the  $\text{CoN}_{\text{pyrr}}\text{C}$  and  $\text{CoN}_{\text{py}}\text{C}$  are 2.02 Å and 1.90 Å, respectively. These bond-length trends align with those reported by others and those from our DFT modeling (**Figure S8**), validating the  $\text{CoN}_{4\text{-pyrrolic}}$  and  $\text{CoN}_{4\text{-pyridinic}}$  in the Co-N-C catalysts.<sup>53,54</sup>

The Wavelet-transform (WT) of EXAFS analysis further elucidates the differences in the coordination environments across the samples, as illustrated in **Figure 2e**. The  $\text{CoN}_{\text{pyrr}}\text{C}$  exhibits a maximum intensity around *ca.* 3.8 Å<sup>-1</sup>, closely aligned with the Co-N path in CoPc. In contrast,  $\text{CoN}_{\text{py}}\text{C}$  displays a maximum intensity at 3.6 Å<sup>-1</sup>, reflecting its different coordination environment compared to  $\text{CoN}_{\text{pyrr}}\text{C}$ .<sup>53</sup> Summarizing the above results, we have experimentally obtained the Co-N-C catalysts with  $\text{CoN}_{4\text{-pyridinic}}$  and  $\text{CoN}_{4\text{-pyrrolic}}$  sites. These samples serve as model catalysts to explore the structure-activity relationship between the Co-N coordination structure and the ORR/HPOR/HPRR and to investigate the connections among these reactions.

### 3.2 2e-ORR/HPOR/HPRR on Co-N-C with $\text{CoN}_{4\text{-pyridinic}}$ and $\text{CoN}_{4\text{-pyrrolic}}$ sites



The Co-N-C catalysts with CoN<sub>4</sub>-pyridinic and CoN<sub>4</sub>-pyrrolic coordination exhibit distinct catalytic properties. In **Figure S6**, the CV reveals comparable capacitive currents for both catalysts, corresponding to similar electrochemical active surface areas of 360.3 m<sup>2</sup>/g for CoN<sub>pyrr</sub>C and 379.8 m<sup>2</sup>/g for CoN<sub>py</sub>C. This surface area equivalence establishes a controlled baseline for subsequent performance comparisons,

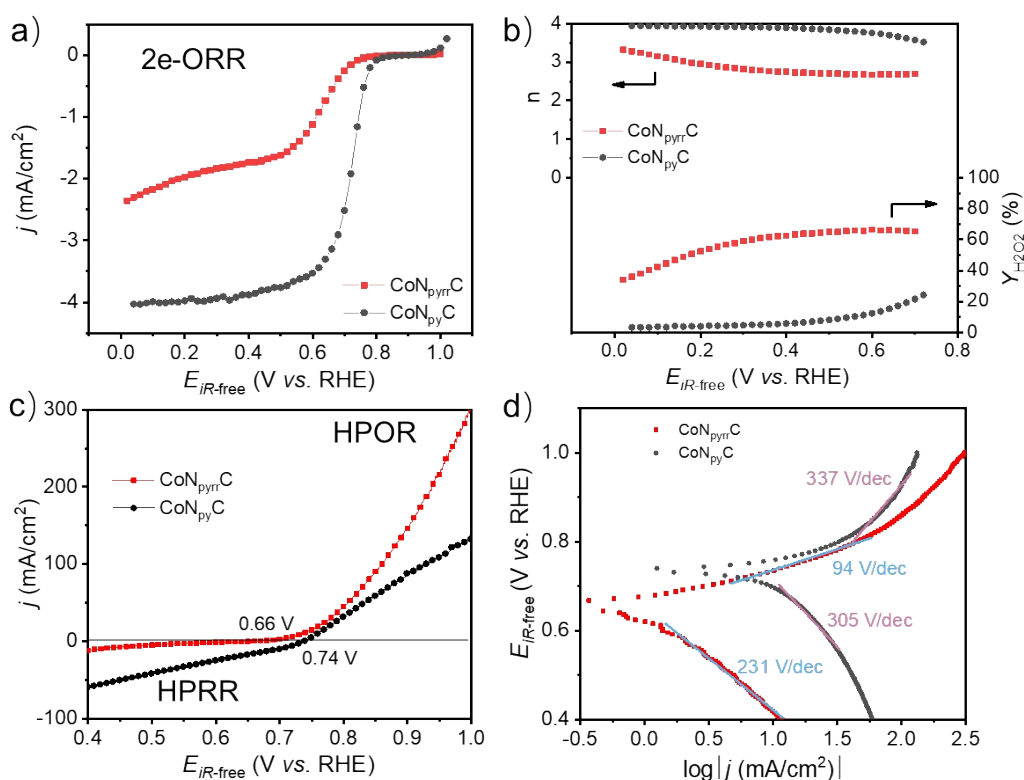


**Figure 3.** a) Steady-state ORR polarization curves, b)  $Y_{H_2O_2}$  and  $n$  in O<sub>2</sub>-saturated 0.5 M H<sub>2</sub>SO<sub>4</sub> by an RRDE system for the CoN<sub>pyrr</sub>C and CoN<sub>py</sub>C. c) Polarization curves recorded at 900 rpm in N<sub>2</sub>-saturated 0.5 M H<sub>2</sub>SO<sub>4</sub> + 0.5 M H<sub>2</sub>O<sub>2</sub> by an H-cell system, and d) Tafel plot of the current density for HPOR measured with the CoN<sub>pyrr</sub>C and CoN<sub>py</sub>C.

eliminating morphological factors as primary contributors to catalytic differences. The steady-state polarization curves in **Figure 3a** highlight that the CoN<sub>pyrr</sub>C exhibits significantly higher 2e-ORR activity than CoN<sub>py</sub>C, with an onset potential ( $E_{onset}$ ) of 0.71 V vs. RHE, closer to the thermodynamic theoretical potential (0.695 V vs. RHE).



The limiting current density ( $j_L$ ) of the CoN<sub>pyrr</sub>C is 2.10 mA/cm<sup>2</sup>, closer to the theoretical  $j_L$  value for 2e-ORR, while that of CoN<sub>py</sub>C is 4.02 mA/cm<sup>2</sup>. **Figure 3b** compares the  $Y_{H_2O_2}$  and  $n$  for these two structures. The maximum  $Y_{H_2O_2}$  for CoN<sub>pyrr</sub>C is *ca.* 66.5% at 0.6 V *vs.* RHE, corresponding to  $n$  around 2.6. The  $Y_{H_2O_2}$  for CoN<sub>py</sub>C is below 12% over the wide voltage range (0-0.6 V *vs.* RHE), with  $n$  close to 4. This result implies that the CoN<sub>4-pyrrolic</sub> coordination is more favorable for 2e-ORR than CoN<sub>4-pyridinic</sub> coordination.

The polarization curves of the two catalysts in an N<sub>2</sub>-saturated solution containing 0.5 M H<sub>2</sub>O<sub>2</sub> and 0.5 M H<sub>2</sub>SO<sub>4</sub> electrolyte are presented in **Figure 3c**. The anodic current at high potential represents the HPOR-dominated process, and the cathodic current at low potential represents the HPRR. When the anode and cathode processes are in equilibrium, the net current becomes zero at the mixing potential ( $U_{mix}$ ).<sup>11,14</sup> For an ideal HPOR catalyst, the  $U_{mix}$  should be close to the thermodynamic equilibrium potential (0.704 V, reversible cell voltage in 0.5 M H<sub>2</sub>SO<sub>4</sub> and 0.5 M H<sub>2</sub>O<sub>2</sub> anolyte) to achieve high efficiency in HPOR. As displayed in **Figure 3c**, the CoN<sub>pyrr</sub>C and CoN<sub>py</sub>C show a  $U_{mix}$  of *ca.* 0.66 and 0.75 V *vs.* RHE. At 1.0 V *vs.* RHE, these catalysts achieve maximum current densities of *ca.* 300 and 130 mA/cm<sup>2</sup>, respectively. Corresponding MA and SA at this potential, detailed in **Table S3**, are 5440 A/g and a SA of 1.51 mA/cm<sup>2</sup> for CoN<sub>pyrr</sub>C versus 1617 A/g and 0.43 mA/cm<sup>2</sup> for CoN<sub>py</sub>C. Furthermore, the calculated Tafel slopes are 94 and 337 mV/dec for CoN<sub>pyrr</sub>C and CoN<sub>py</sub>C, respectively, based on the Tafel equation (*Eq.6*) (**Figure 3d**). The CoN<sub>pyrr</sub>C exhibits significantly higher HPOR activity compared to the CoN<sub>py</sub>C. We assume that the CoN<sub>4-pyrrolic</sub> is the active site for the HPOR process.

For the HPRR process, CoN<sub>py</sub>C exhibits significantly higher activity than the CoN<sub>pyrr</sub>C catalyst. At 0.4 V *vs.* RHE, the CoN<sub>py</sub>C catalyst achieves a current density of *ca.* 62 mA/cm<sup>2</sup>, much higher than that of the CoN<sub>pyrr</sub>C (*ca.* 10 mA/cm<sup>2</sup>). This enhanced activity is reflected in the MA and SA values at 0.4 V *vs.* RHE. CoN<sub>py</sub>C achieves a markedly higher MA of 675 A/g and SA of 0.18 mA/cm<sup>2</sup>, while CoN<sub>pyrr</sub>C displays an



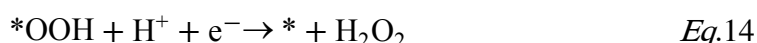
MA of 119.8 A/g and SA of 0.03 mA/cm<sup>2</sup> (Table S3). Despite this superior activity, CoN<sub>py</sub>C displays a larger Tafel slope (305 mV/dec) compared to the CoN<sub>pyrr</sub>C (231 mV/dec). It is noteworthy that both CoN<sub>py</sub>C and CoN<sub>pyrr</sub>C catalysts exhibit large Tafel slopes for HPRR. Tafel slopes larger than 120 mV/dec are typically associated with a chemical-electrochemical mechanism in which the chemical step is rate-determining.<sup>23</sup> Overall, the CoN<sub>4-pyrrolic</sub> coordination shows high activity for 2e-ORR/HPOR, whereas CoN<sub>4-pyridinic</sub> coordination exhibits preferred HPRR. Critical control experiments with negligible ORR/HPOR/HPRR activity for N<sub>pyrr</sub>C and N<sub>py</sub>C blank N-doped carbon matrices (**Figure S7**) further confirm that the catalytic activity difference is predominantly due to the variation in CoN<sub>4</sub> coordination environment rather than morphological features or residual metals.

**Table S4** provides a benchmark comparison of our CoN<sub>py</sub>C and CoN<sub>pyrr</sub>C catalysts with selected CoN<sub>4</sub>-based catalysts reported in prior studies.<sup>15,35,55,56</sup> It appears that the high 2e-ORR is accompanied by high HPOR and low HPRR, while 4e-ORR occurs, it is typically accompanied by acceptable HPOR and HPRR. Subsequent DFT calculations will provide further insight into the correlation among these reactions.

### 3.3 Theoretical calculation on 2e-ORR/HPOR/HPRR.

DFT calculations were performed to understand the structure-activity relationship between CoN<sub>4</sub> catalysts with CoN<sub>4-pyridinic</sub> and CoN<sub>4-pyrrolic</sub> coordination and the 2e-ORR/HPOR/HPRR. We built the CoN<sub>4-pyrrolic</sub> and CoN<sub>4-pyridinic</sub> models and optimized their structures. The optimized lattice parameters and Co-N bond length are shown in Figure S8. The detailed calculation data for all species are displayed in **Table S5**.

For 2e-ORR, the generally accepted pathway in acid is as follows<sup>34, 57</sup>:



This pathway is composed of two consecutive proton-coupled electron transfer (PCET) steps, involving a single intermediate,  $^*\text{OOH}$ . However, the chemisorption of oxygen ( $^* + \text{O}_2 \rightarrow ^*\text{O}_2$ ) and the desorption of  $\text{H}_2\text{O}_2$  are not considered in this pathway, and the reason is not well documented.<sup>32</sup> Therefore, we first remodeled the 2e-ORR pathways on the  $\text{CoN}_{4\text{-pyrrolic}}$  and  $\text{CoN}_{4\text{-pyridinic}}$  surfaces by considering the  $\text{O}_2$ -adsorption and  $\text{H}_2\text{O}_2$ -desorption steps and compared the results with the conventional 2e-ORR pathway model. The remodeled pathway is as follows:

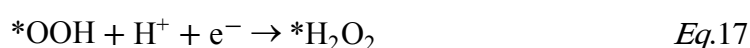


**Figure 4a** shows the reaction free energy diagrams of these pathways at  $U = 0.695$  V. The optimized structures of the intermediates are shown in **Figure S9**. We found that the strong binding of  $^*\text{O}_2$  at the  $\text{CoN}_{4\text{-pyridinic}}$  site creates a high barrier for the next reduction step of  $^*\text{O}_2$  to  $^*\text{OOH}$ , which would negatively affect both 4e-ORR and 2e-ORR activity (dashed line in **Figure 4a**), while the slightly weak binding of  $^*\text{O}_2$  at the  $\text{CoN}_{4\text{-pyrrolic}}$  site can be easily overcome. However, this prediction is not consistent with the observed high 4e-ORR activity of the  $\text{CoN}_{\text{py}}\text{C}$  catalyst in our experiment. Alternatively, considering the  $\text{O}_2$  gas, dissolved  $\text{O}_2$ , and  $^*\text{O}_2$  are at equilibrium (0.695 V) and therefore have the same chemical potential, the free energy  $^*\text{O}_2$  at equilibrium (rather than at the  $\text{O}_2$  coverage used in the DFT model) can be replaced with that of free  $\text{O}_2$ . With this treatment, the conventional pathway model predicts higher 2e-ORR activity of  $\text{CoN}_{4\text{-pyrrolic}}$  than  $\text{CoN}_{4\text{-pyridinic}}$  (solid line in **Figure 4a**). In this case, the removal of  $^*\text{OOH}$  is slightly uphill, and it serves as the rate-determining step (RDS) for both  $\text{CoN}_{4\text{-pyrrolic}}$  and  $\text{CoN}_{4\text{-pyridinic}}$ . The  $\text{CoN}_{4\text{-pyrrolic}}$  exhibits a lower thermodynamic



onset overpotential ( $\eta$ ,  $\eta_{2e-ORR} = 0.06$  V) compared to the CoN<sub>4-pyridinic</sub> ( $\eta_{2e-ORR} = 0.25$  V), indicating that the CoN<sub>4-pyrrolic</sub> has a higher 2e-ORR activity than CoN<sub>4-pyridinic</sub>.

**Figure 4b** shows the volcano-type relationship between the thermodynamic limiting potential ( $U_L$ ) and the binding free energy of \*OOH ( $\Delta G^*_{OOH}$ ) and the predicted values for CoN<sub>4-pyrrolic</sub> and CoN<sub>4-pyridinic</sub>. The left region of the plot represents the strong binding of \*OOH, while the right downhill part in the volcano plot corresponds to the weak binding of \*OOH. The volcano reaches its peak at the equilibrium potential at 0.695 V with the optimal  $\Delta G^*_{OOH}$  of 4.225 eV. The CoN<sub>4-pyrrolic</sub> shows  $\Delta G^*_{OOH}$  of 4.16 eV, which is close to the optimal value, indicating that CoN<sub>4-pyrrolic</sub> prefers the 2e-ORR process. This prediction agrees with the observed low  $E_{onset}$  of 2e-ORR for the CoN<sub>pyr</sub>C catalyst in Figure 3a. Furthermore, we also investigated the electron transfer between the \*OOH intermediate and these two types of CoN<sub>4</sub> sites by Bader charge analysis, which determines the binding strength of the \*OOH intermediate. As shown in **Figure S10**, the CoN<sub>4-pyrrolic</sub> site transfers less charge (0.28 e) to the \*OOH intermediate than the CoN<sub>4-pyridinic</sub> site (0.35 e), which leads to the weaker binding of \*OOH at the CoN<sub>4-pyrrolic</sub> site. The good agreement between the experimental and theoretical results indicates that  $\Delta G^*_{OOH}$  is a suitable activity descriptor for 2e-ORR at these CoN<sub>4</sub> sites. Therefore, deliberate engineering of CoN<sub>4-pyrrolic</sub> sites, guided by the  $\Delta G^*_{OOH}$  descriptor, provides a strategic pathway to design highly active catalysts for H<sub>2</sub>O<sub>2</sub> production.

On the other hand, the HPOR is the reverse 2e-ORR process involving the same intermediate, and its pathway is as follows:

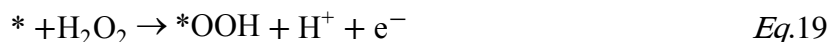


**Figure 4a** shows the calculated reaction free energy diagrams of the HPOR (inverse process of 2e-ORR) at 0.695 V. In the conventional pathway model, without considering the \*O<sub>2</sub> and \*H<sub>2</sub>O<sub>2</sub>, the RDS of HPOR for both CoN<sub>4-pyrrolic</sub> and CoN<sub>4-pyridinic</sub> is the removal of \*OOH, due to the uphill energy required for converting \*OOH to O<sub>2</sub>.



The CoN<sub>4</sub>-pyrrolic exhibits  $\eta_{\text{HPOR}}$  of 0.06 V, lower than 0.25 V predicted for the CoN<sub>4</sub>-pyridinic, indicating its higher HPOR than the CoN<sub>4</sub>-pyridinic. If considering the \*O<sub>2</sub> and \*H<sub>2</sub>O<sub>2</sub> states, the model predicts O<sub>2</sub> desorption as the RDS for HPOR at CoN<sub>4</sub>-pyridinic and its lower activity than CoN<sub>4</sub>-pyrrolic.

**Figure 4b** shows the relationship between the  $U_L$  of the HPOR and  $\Delta G^*_{\text{OOH}}$ . An optimal HPOR catalyst should have a  $\Delta G^*_{\text{OOH}}$  of 4.225 eV, and the corresponding  $U_L$  should be close to the equilibrium potential (0.695 V) with minimized overpotential. The CoN<sub>4</sub>-pyrrolic demonstrates a  $\Delta G^*_{\text{OOH}}$  of 4.16 eV with a  $U_L$  of 0.76 V, which is near the theoretical equilibrium potential. While the CoN<sub>4</sub>-pyridinic has a  $\Delta G^*_{\text{OOH}}$  of 3.97 eV, and the corresponding  $U_L$  is 0.95 V. These results are consistent with the higher HPOR activity of CoN<sub>pyrr</sub>C than CoN<sub>py</sub>C (Figure 3c). Consequently,  $\Delta G^*_{\text{OOH}}$  serves as a thermodynamic activity descriptor for both the HPOR and 2e-ORR at CoN<sub>4</sub> sites. The superior HPOR and 2e-ORR demonstrated by CoN<sub>4</sub>-pyrrolic sites enable an efficient electrochemical cycle of H<sub>2</sub>O<sub>2</sub>, offering potential applications in energy and hydrogen storage.<sup>11,13,14</sup>





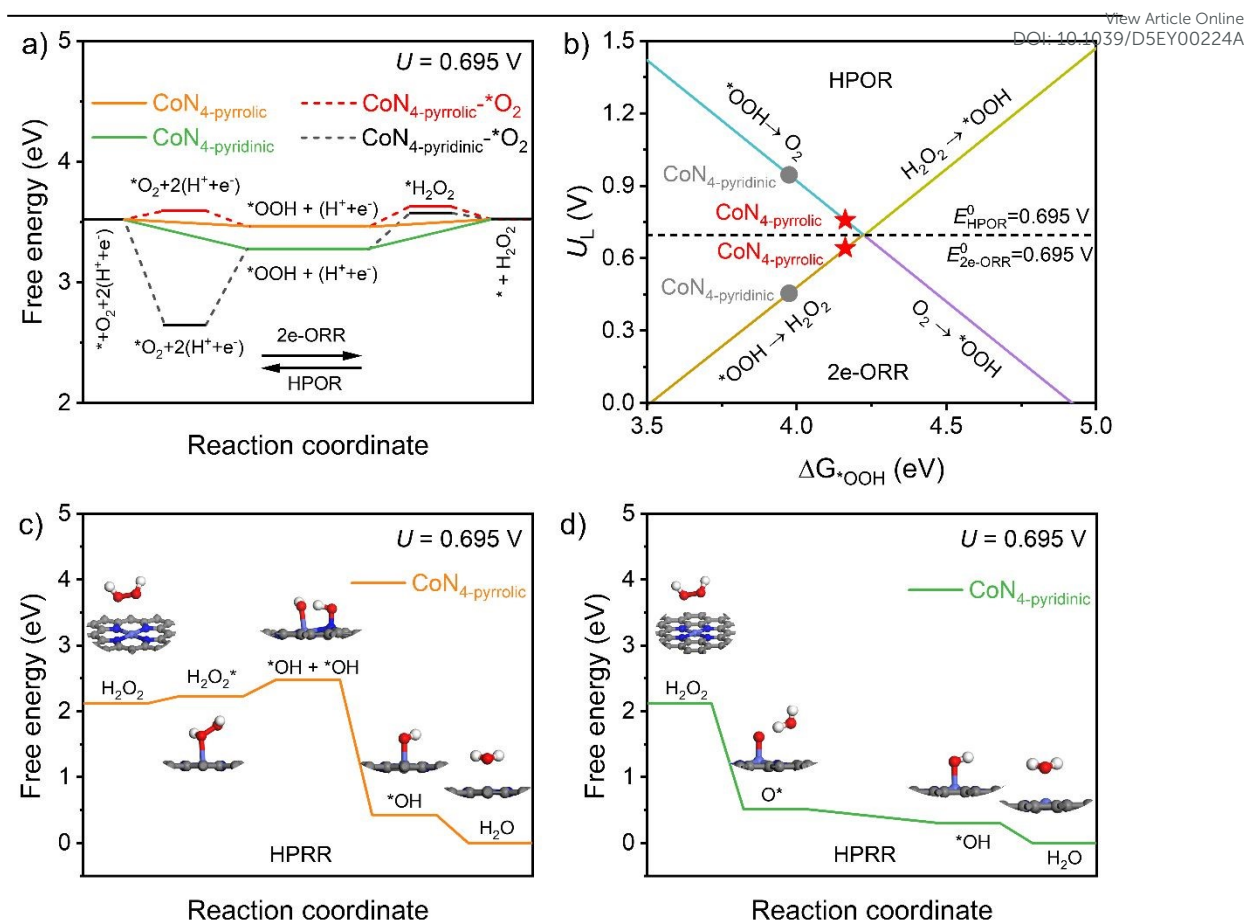


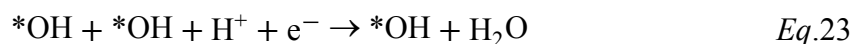
**Figure 4.** a) Free energy diagram of 2e-ORR/HPOR on the CoN<sub>4</sub>-pyrrolic and CoN<sub>4</sub>-pyridinic. The dash line represents 2e-ORR/HPOR process including the chemisorption of reactants. b) Volcano plot for the  $U_L$  of the 2e-ORR/HPOR against  $\Delta G_{^*OOH}$  on the CoN<sub>4</sub>-pyrrolic and CoN<sub>4</sub>-pyridinic. c) Free energy diagram for HPRR on the CoN<sub>4</sub>-pyrrolic, along with the optimized structures of intermediates involved in HPRR process on the CoN<sub>4</sub>-pyrrolic. d) Free energy diagram for HPRR on the CoN<sub>4</sub>-pyrrolic, and the optimized structures of intermediates.

For HPRR, no general pathway has been proposed so far. The Tafel slopes observed in our results and reported for various catalysts exceed 120 mV/dec, which are very large and typical for chemical-electrochemical mechanisms.<sup>23,58,59</sup> Therefore,





we propose the following possible chemical-electrochemical HPRR pathways on the CoN<sub>4</sub>-pyrrolic and CoN<sub>4</sub>-pyridinic. On the CoN<sub>4</sub>-pyrrolic, the HPRR is as follows:



The HPRR on the CoN<sub>4</sub>-pyridinic is as follows:



where Eq.21 and Eq.22 are the chemical pathways, Eq.23 and Eq.24 are the electrochemical pathways on the CoN<sub>4</sub>-pyrrolic; Eq.25 is the chemical pathway, Eq.26 and Eq.27 are the electrochemical pathways on the CoN<sub>4</sub>-pyridinic.

**Figure 4c-d** shows the complete HPRR pathways and calculated reaction free energy diagram at  $U = 0.695$  V for both CoN<sub>4</sub>-pyrrolic and CoN<sub>4</sub>-pyridinic (**Figure S11** for  $U = 0$  V). On the CoN<sub>4</sub>-pyrrolic, H<sub>2</sub>O<sub>2</sub> adsorbs on top of the Co atom via the O atom (**Figure S12**), and then dissociates to two \*OH via HO–OH scission, which is an endothermic chemical reaction. Subsequently, these two \*OH combine with two (H<sup>+</sup> + e<sup>−</sup>) pairs to form two H<sub>2</sub>O molecules, which is characterized by significant exothermicity. The RDS of this pathway is the HO–OH scission step, with an energy barrier exceeding 0.25 eV, in line with the chemical-electrochemical mechanism suggested by Tafel slope analyses (Figure 3d). In contrast, H<sub>2</sub>O<sub>2</sub> undergoes spontaneous dissociation on the CoN<sub>4</sub>-pyridinic (**Figure S13**), resulting in the formation of \*O and H<sub>2</sub>O. The \*O combines with one (H<sup>+</sup> + e<sup>−</sup>) pair, forming \*OH, followed by a second (H<sup>+</sup> + e<sup>−</sup>) pair and forming H<sub>2</sub>O. This pathway is entirely exothermic, with the RDS being the



electrochemical removal of  $\ast\text{OH}$ . Consequently, at  $U = 0.695$  V, the HPRR activity on the  $\text{CoN}_{4\text{-pyridinic}}$  is thermodynamically more favorable than that on the  $\text{CoN}_{4\text{-pyrrolic}}$  surface, which aligns well with the observed activity order in Figure 3c. Furthermore, the simple electrochemical process involving only the  $\ast\text{OH}$  intermediate is also calculated to compare the HPRR activity (**Figure S14**). Therefore, DFT calculations and Tafel slope analysis validate the chemical-electrochemical mechanism for the HPRR on both  $\text{CoN}_{4\text{-pyrrolic}}$  and  $\text{CoN}_{4\text{-pyridinic}}$ . This leads to the conclusion that the  $\Delta G_{\ast\text{OH}}$  cannot serve as a reliable descriptor for HPRR. As the first atomistic-level elucidation of HPRR pathways on  $\text{CoN}_4$  catalysts, this work provides fundamental insights for designing cathode catalysts in direct  $\text{H}_2\text{O}_2$  fuel cells.<sup>6-10</sup>

It is important to note that the free energy diagram indicates that  $\text{CoN}_{4\text{-pyrrolic}}$  and  $\text{CoN}_{4\text{-pyridinic}}$  exhibit lower overpotentials ( $\eta_{\text{HPRR}} < 0.5$  V) for HPRR, which deviates from the experimental results ( $\eta_{\text{HPRR}} \approx 1$  V). This discrepancy arises from the limitations of computational methods like DFT, which focus on thermodynamics but overlook kinetic barriers crucial for reaction rates, such as proton-electron transfer. Additionally, DFT may not accurately represent realistic surface coverages of reactants or intermediates, affecting the energetics of key reaction steps. Thus, while DFT and experimental data agree on the trend that HPRR is thermodynamically favorable on  $\text{CoN}_{4\text{-pyridinic}}$  surfaces, factors like reaction kinetics and surface coverage lead to higher observed overpotentials than predicted by DFT.

Our detailed theoretical investigation on  $\text{CoN}_{4\text{-pyrrolic}}$  and  $\text{CoN}_{4\text{-pyridinic}}$  elucidates the critical role of the  $\ast\text{OOH}$  intermediate as a descriptor for both the 2e-ORR and HPOR activities. The  $\text{CoN}_{4\text{-pyrrolic}}$  type structure exhibits higher 2e-ORR/HPOR activity than the  $\text{CoN}_{4\text{-pyridinic}}$  type structure due to its more optimal  $\Delta G_{\ast\text{OOH}}$ . The HPRR pathway analysis offers insights that the oversimplified use of  $\Delta G_{\ast\text{OH}}$  as a descriptor might fail to depict chemical-electrochemical mechanisms accurately. The significant differences in HPRR pathways on  $\text{CoN}_{4\text{-pyrrolic}}$  and  $\text{CoN}_{4\text{-pyridinic}}$  originate from  $\text{H}_2\text{O}_2$  adsorption and thermodynamic energies. The  $\text{CoN}_{4\text{-pyrrolic}}$  type structure demonstrates



inferior catalytic activity in HPRR compared to the  $\text{CoN}_{4\text{-pyridinic}}$  type structure, attributable to a higher chemical dissociation barrier of  $\text{H}_2\text{O}_2$ , while  $\text{H}_2\text{O}_2$  spontaneously dissociates on the  $\text{CoN}_{4\text{-pyridinic}}$ . Thus,  $\Delta G^*_{\text{OOH}}$  can serve as a descriptor for 2e-ORR/HPOR activities, but not for the HPRR, which requires a more detailed consideration of the chemical reaction steps involved. For electrochemical  $\text{H}_2\text{O}_2$  synthesis, we propose targeting  $\text{CoN}_{4\text{-pyrrolic}}$  sites while tuning  $\Delta G^*_{\text{OOH}}$  toward optimal values (4.225 eV) through coordination engineering. Conversely, for  $\text{H}_2\text{O}_2$  fuel cell cathodes requiring efficient HPRR, catalyst design should prioritize  $\text{CoN}_{4\text{-pyridinic}}$  configurations that facilitate spontaneous  $\text{H}_2\text{O}_2$  dissociation and optimize  $^*\text{OH}$  binding energetics. These site-specific design principles enable the rational development of integrated systems where  $\text{H}_2\text{O}_2$  serves as both an energy carrier (in production) and a fuel (in consumption).

#### 4. Conclusion

We explored the intrinsic relationship between 2e-ORR/HPOR/HPRR using two model Co-N-C catalysts with  $\text{CoN}_4$  sites in different coordination environments. The Co-N-C catalyst with  $\text{CoN}_{4\text{-pyrrolic}}$  sites exhibits higher 2e-ORR and HPOR activity than that with  $\text{CoN}_{4\text{-pyridinic}}$  sites, while the latter shows higher HPRR activity. Computational results indicate that the superior 2e-ORR/HPOR activity of the  $\text{CoN}_{4\text{-pyrrolic}}$  site originates from its more optimal  $\Delta G^*_{\text{OOH}}$  value. The HPRR activity of the  $\text{CoN}_4$  sites are determined by the chemical adsorption step of  $\text{H}_2\text{O}_2$ . The  $\text{CoN}_{4\text{-pyrrolic}}$  exhibits a high  $\text{H}_2\text{O}_2$  dissociation barrier that hinders HPRR, whereas  $\text{H}_2\text{O}_2$  spontaneously dissociates on the  $\text{CoN}_{4\text{-pyridinic}}$ , leading to higher HPRR activity. These results suggest that  $\Delta G^*_{\text{OOH}}$  can serve as a descriptor for 2e-ORR/HPOR activities, but not for the HPRR, which needs to take the chemical reaction steps into consideration. These results can provide valuable insights into the  $\text{H}_2\text{O}_2$ -related reactions and guide the development of high-performance catalysts for various  $\text{H}_2\text{O}_2$ -based energy conversion and storage applications.



**Corresponding Author**

\* Lifang Chen -*State Key Laboratory of Coal Conversion, Institute of Coal Chemistry, Chinese Academy of Sciences; Taiyuan, Shanxi 030001, China.*

Email: chenlifang@sxicc.ac.cn

\* Ruimin Ding -*State Key Laboratory of Coal Conversion, Institute of Coal Chemistry, Chinese Academy of Sciences; Taiyuan, Shanxi 030001, China.*

Email: dingrm@sxicc.ac.cn

\* Lin Gan- *Tsinghua Shenzhen International Graduate School, Tsinghua University, Shenzhen 518055, China*

Email: lgan@sz.tsinghua.edu.cn

\* Xi Yin-*State Key Laboratory of Coal Conversion, Institute of Coal Chemistry, Chinese Academy of Sciences; Taiyuan, Shanxi 030001, China.*

Email: xiyin@sxicc.ac.cn

**CRedit authorship contribution statement**

**Jie Yang:** Writing - Original Draft, Methodology, Investigation, Visualization. **Lifang Chen:** Methodology, Investigation, Visualization, Supervision. **Xuya Zhu:** Investigation, Visualization. **Wenwen Shi:** Investigation, Visualization. **Mengxue Huang:** Investigation, Visualization. **Chang Liu:** Investigation, Visualization. **Ruimin Ding:** Writing - Review & Editing, Supervision, Funding acquisition. **Lin Gan:** Writing - Review & Editing, Supervision, Funding acquisition. **Xi Yin:** Conceptualization, Methodology, Writing - Review & Editing, Supervision, Funding acquisition.

**Declaration of competing interest**

The authors declare no conflict of interest.

**Supporting Information**

Supplementary data associated with this article can be found in the Supporting Information

View Article Online  
DOI: 10.1039/D5EY00224A

## Acknowledgment

This study was financially supported by the national Key Research and development Program of China grant (Grant No. 2021YFB4001203), the Shanxi Province grant (Grant No. 202203021212007) and the autonomous research project of SKLCC (Grant No. SCJC-HN-2023-16 and SCJC-HN-2023-17). The authors wish to thank the facility's support of the 4B9A beamline of the Beijing Synchrotron Radiation Facility (BSRF) and BL14W1 beamline of Shanghai Institute of Applied Physics (SINAP).

## References

1. C. Xia, Y. Xia, P. Zhu, L. Fan, H. Wang, *Science*, **2019**, 366, 226-231.
2. Z. Lu, G. Chen, S. Siahrostami, Z. Chen, K. Liu, J. Xie, L. Liao, T. Wu, D. Lin, Y. Liu, T. F. Jaramillo, J. K. Nørskov, Y. Cui, *Nat. Catal.*, **2018**, 1, 156-162.
3. H. Kim, M. Ross, N. Kornienko, L. Zhang, J. Guo, P. Yang, B. McCloskey, *Nat. Catal.*, **2018**, 1, 282-290.
4. J. Qi, Y. Du, Q. Yang, N. Jiang, J. Li, Y. Ma, Y. Ma, X. Zhao, J. Qiu, *Nat. Commun.*, **2023**, 14, 6263.
5. L. Jing, W. Wang, Q. Tian, Y. Kong, X. Ye, H. Yang, Q. Hu, C. He, *Angew. Chem. Int. Edit.* **2024**, 63, e202403023.
6. C. J. McDonnell-Worth, D. R. MacFarlane, *Aust. J. Chem.*, **2018**, 71, 781-788.
7. Y. Yang, R. Dong, Y. Zhu, H. Li, H. Zhang, X. Fan, H. Chang, *Chem. Eng. J.*, **2020**, 381, 122749.
8. F. Yang, K. Cheng, X. Liu, S. Chang, J. Yin, C. Du, L. Du, G. Wang, D. Cao, *J. Power Sources*, **2012**, 217, 569-573.
9. A. E. Sanli, A. Aytaç, *Int. J. Hydrogen Energy*, **2011**, 36, 869-875.



10. L. An, T. Zhao, X. Yan, X. Zhou, P. Tan, *Sci. Bull.*, **2015**, 60, 55-64.
11. J. Yang, R. Ding, C. Liu, S. Liu, Q. Xu, L. Chen, J. Chen, J. Li, X. Yin, *J. Power Sources*, **2022**, 545, 231948.
12. R. Disselkamp, *Int. J. Hydrogen Energy*, **2010**, 35, 1049-1053.
13. J. Yang, R. Ding, C. Liu, L. Chen, Q. Wang, S. Liu, Q. Xu, X. Yin, *Green Chem.*, **2024**, 26, 7769-7778.
14. C. Liu, R. Ding, J. Yang, S. Liu, L. Chen, Q. Xu, J. Li, X. Yin, *ACS Sustain. Chem. Eng.*, **2023**, 11, 2599-2606.
15. Y. Sun, L. Silvoli, N. R. Sahraie, W. Ju, J. Li, A. Zitolo, S. Li, A. Bagger, L. Arnarson, X. Wang, T. Moeller, D. Bernsmeier, J. Rossmeisl, F. Jaouen, P. Strasser, *J. Am. Chem. Soc.*, **2019**, 141, 12372-12381.
16. Y. Sun, S. Li, Z. P. Jovanov, D. Bernsmeier, H. Wang, B. Paul, X. Wang, S. Kuhl, P. Strasser, *ChemSusChem*, **2018**, 11, 3388-3395.
17. C. H. Choi, H. Lim, M. Chung, G. Chon, N. Ranjbar, A. Altin, M. Sougrati, L. Stievano, H. Oh, E. Park, F. Luo, P. Strasser, G. Drazic, K. Mayrhofer, H. Kim, F. Jaouen, *Energy Environ. Sci.*, **2018**, 11, 3176-3182.
18. J. Wu, X. Yuan, J. Martin, H. Wang, J. Zhang, J. Shen, S. Wu, W. Merida, *J. Power Sources*, **2008**, 184, 104-119.
19. S. Siahrostami, A. Verdager, M. Karamad, D. Deiana, P. Malacrida, B. Wickman, M. Escudero, E. Paoli, R. Frydendal, T. Hansen, I. Chorkendorff, I. Stephens, J. Rossmeisl, *Nat. Mater.*, **2013**, 12, 1137-1143.
20. J. Lim, Y. Sa, S. Joo, *Cell Rep. Phys. Sci.*, **2022**, 3, 100987.
21. J. Lee, B. Lee, Y. Lee, A. Kim, D. Lee, H. Lim, H. Song, *Small*, **2023**, 19, 2303263.
22. K. Deng, W. Wang, Q. Mao, H. Yu, Z. Wang, Y. Xu, X. Li, H. Wang, L. Wang, *Small*, **2022**, 18, 2203020.
23. K. Stewart, A. Gewirth, *Langmuir*, **2007**, 23, 9911-9918.
24. V. Briega, E. Herrero, J. Feliu, *Chinese J. Catal.*, **2020**, 41, 732-738.



25. I. Katsounaros, W. Schneider, J. Meier, U. Benedikt, P. Biedermann, A. Auer, K. Mayrhofer, *Phys. Chem. Chem. Phys.*, **2012**, 14, 7384-7391.
26. R. Rizo, J. Feliu, E. Herrero, *Chin. J. Catal.*, **2021**, 398, 123-132.
27. S. Deshpande, J. Kitchin, V. Viswanathan, *ACS Catal.*, **2016**, 6, 5251-5259.
28. G. Luque, M. Rojas, G. Rivas, E. Leiva, *Electrochim. Acta*, **2010**, 56, 523-530.
29. S. Shi, J. Yang, L. Chen, M. Huang, C. Liu, R. Ding, X. Yin, *J. Electrochem. Soc.*, **2024**, 171, 046504.
30. X. Li, D. Heryadi, A. Gewirth, *Langmuir*, **2005**, 21, 9251-9259.
31. F. Calle, J. Martínez, J. Rossmeisl, *Phys. Chem. Chem. Phys.*, **2011**, 13, 15639-15643.
32. A. Kulkarni, S. Siahrostami, A. Patel, J. Nørskov, *Chem. Rev.*, **2018**, 118, 2302-2312.
33. K. Exner, *Chem Catal.*, **2021**, 1, 258-271.
34. Z. Seh, J. Kibsgaard, C. Dickens, I. Chorkendorff, J. Nørskov, T. Jaramillo, *Science*, **2017**, 355, eaad4998.
35. F. Jaouen, J. Dodelet, *J. Phy. Chem. C*, **2009**, 113, 15422-15432.
36. S. Chen, T. Luo, X. Li, K. Chen, J. Fu, K. Liu, C. Cai, Q. Wang, H. Li, Y. Chen, C. Ma, L. Zhu, Y. Lu, T. Chan, M. Zhu, E. Cortes, M. Liu, *J. Am. Chem. Soc.*, **2022**, 144, 14505-14516.
37. Perdew, J.; Burke, K.; Ernzerhof, M., *Phys. Rev. Lett.*, **1996**, 77, 3865-3868.
38. G. Kresse, J. Furthmüller, *Comput. Mater. Sci.*, **1996**, 6, 15-50.
39. G. Kresse, J. Furthmüller, *Phys. Rev. B.*, **1996**, 54, 11169-11186.
40. P. Blöchl, *Phys. Rev. B.*, **1994**, 50, 17953-17979.
41. G. Kresse, D. Joubert, *Phys. Rev. B.*, **1999**, 59, 1758-1775.
42. S. Grimme, J. Antony, S. Ehrlich, H. Krieg, *J. Chem. Phys.*, **2010**, 132, 154104.
43. J. Nørskov, J. Rossmeisl, A. Logadottir, L. Lindqvist, J. Kitchin, T. Bligaard, H. Jónsson, *J. Phys. Chem. B*, **2004**, 108, 17886-17892.



44. F. Calle-Vallejo, J. Martínez, J. Rossmeisl, *Phys. Chem. Chem. Phys.*, **2011**, 13, 15639-15643.
45. X. Yin, H. Chung, U. Martinez, L. Lin, K. Artyushkova, P. Zelenay, *J. Electrochem. Soc.*, **2019**, 166, F3240.
46. X. Ao, Y. Ding, G. Nam, L. Soule, P. Jing, B. Zhao, J. Hwang, J. Jang, C. Wang, M. Liu, *Small*, **2022**, 18, 2203326.
47. K. Artyushkova, B. Kiefer, B. Halevi, A. Knop-Gericke, R. Schlögl, P. Atanassov, *Chem. Commun.*, **2013**, 49, 2539-2541.
48. J. Wang, Y. Huang, Y. Wang, H. Deng, Y. Shi, D. Wei, M. Li, , C. Dong, H. Jin, S. Mao, S. Shen, *ACS Catal.*, **2023**, 13, 2374-2385.
49. Y. Tian, M. Li, Z. Wu, Q. Sun, D. Yuan, B. Johannessen, L. Xu, Y. Wang, Y. Dou, H. Zhao, S. Zhang, *Angew. Chem. Int. Ed.*, **2022**, 61, e202213296.
50. Y. He, H. Guo, S. Hwang, X. Yang, Z. He, J. Braaten, S. Karakalos, W. Shan, M. Wang, H. Zhou, Z. Feng, K. L. More, G. Wang, D. Su, D. A. Cullen, L. Fei, S. Litster, G. Wu, *Adv. Mater.*, **2020**, 32, 2003577.
51. Y. Han, Y.-G. Wang, W. Chen, R. Xu, L. Zheng, J. Zhang, J. Luo, R.-A. Shen, Y. Zhu, W.-C. Cheong, C. Chen, Q. Peng, D. Wang, Y. Li, *J. Am. Chem. Soc.*, **2017**, 139, 17269-17272.
52. Y. Sa, S. Park, G. Jung, T. Shin, H. Jeong, S. Kwak, S. Joo, *ACS Catal.*, **2019**, 9, 83-97.
53. H. Zhuang, T. Zhang, H. Xiao, F. Zhang, P. Han, H. Gu, J. Jiao, W. Chen, Q. Gao, *Appl. Catal. B-Environ.*, **2024**, 340, 123273.
54. Y. Cheng, J. Peng, G. Lai, X. Yue, F. Li, Q. Wang, L. Chen, J. Gu, *ACS Catal.*, **2024**, 14, 8446-8455.
55. J. Lee, B. Lee, Y. Lee, A. Kim, D. Lee, H. Lim, H.-K. Song, *Small*, **2023**, 19, 2303263.
56. J. Gao, H. Yang, X. Huang, S.-F. Hung, W. Cai, C. Jia, S. Miao, H. Chen, X. Yang, Y. Huang, T. Zhang, B. Liu, *Chem*, **2020**, 6, 658-674.





- 
57. X. Sun, K. Li, C. Yin, Y. Wang, M. Jiao, F. He, X. Bai, H. Tang, Z. Wu, *Carbon*, **2016**, 108, 541-550. View Article Online  
DOI: 10.1039/D5EY00224A
58. P. Balbuena, S. Calvo, E. Lamas, P. Salazar, J. Seminario, *J. Phys. Chem. B*, **2006**, 110, 17452-17459.
59. M. Eslamibidgoli, M. Eikerling, *ACS Catal.*, **2015**, 5, 6090-6098.



Data availability statements

[View Article Online](#)  
DOI: 10.1039/D5EY00224A

The data supporting this article have been included as part of the Supplementary Information.

